Electrostatic influence on IL-1 transport through the GSDMD pore

Wen Jun Xie[a,1], Shiyu Xia[b,c,1], Arieh Warshel[a,2], and Hao Wu[b,c,2]

[a]Department of Chemistry, University of Southern California, Los Angeles, CA 90089; [b]Department of Biological Chemistry and Molecular Pharmacology, Harvard Medical School, Boston, MA 02115; and [c]Program in Cellular and Molecular Medicine, Boston Children's Hospital, Boston, MA 02115

Contributed by Hao Wu; received November 5, 2021; accepted January 3, 2022; reviewed by Michael Grabe and Yinghao Wu

A variety of signals, including inflammasome activation, trigger the formation of large transmembrane pores by gasdermin D (GSDMD). There are primarily two functions of the GSDMD pore, to drive lytic cell death, known as pyroptosis, and to permit the release of leaderless interleukin-1 (IL-1) family cytokines, a process that does not require pyroptosis. We are interested in the mechanism by which the GSDMD pore channels IL-1 release from living cells. Recent studies revealed that electrostatic interaction, in addition to cargo size, plays a critical role in GSDMD-dependent protein release. Here, we determined computationally that to enable electrostatic filtering against pro-IL-1β, acidic lipids in the membrane need to effectively neutralize positive charges in the membrane-facing patches of the GSDMD pore. In addition, we predicted that salt has an attenuating effect on electrostatic filtering and then validated this prediction using a liposome leakage assay. A calibrated electrostatic screening factor is necessary to account for the experimental observations, suggesting that ion distribution within the pore may be different from the bulk solution. Our findings corroborate the electrostatic influence of IL-1 transport exerted by the GSDMD pore and reveal extrinsic factors, including lipid and salt, that affect the electrostatic environment.

gasdermin D | interleukin-1 | electrostatics | inflammasome | channel

Gasdermins (GSDMs) are a family of pore-forming proteins with profound implications in innate immunity, inflammatory diseases, and antitumor immunity (1–5). Inactive GSDMs are monomeric cytosolic proteins with a functional N-terminal domain (NT) repressed by an autoinhibitory C-terminal domain (CT) (6, 7). Under diverse cellular conditions, many enzymes, including caspases and granzymes, can proteolytically activate GSDMs by cleaving off GSDM-CT to liberate GSDM-NT for pore formation on the plasma membrane and possibly other biological membranes (1, 8, 9). GSDMD, the prototypical member of the family, was discovered as a substrate of inflammatory caspases activated by inflammasomes in response to host sensing of pathogens or sterile danger signals (10–12).

Studies so far have demonstrated pyroptosis and hyperactivation as two major cellular consequences of GSDMD activation. Formation of GSDMD pores causes ionic fluxes and may eventually drive membrane rupture (13, 14). This mode of lytic cell death is termed pyroptosis, which is highly inflammatory and immunogenic due to the leakage of cytosolic contents through lysed membranes (15). On the other hand, cells may survive a modest degree of GSDMD pore formation due to membrane-repair mechanisms, weak inflammasome activation, and stimulation by oxidized lipids (16–18). In this state known as hyperactivation, cells do not undergo pyroptosis, but contain actively signaling inflammasomes that process interleukin-1β (IL-1β) and IL-18 and GSDMD pores that release these cytokines (19, 20).

In both pyroptotic and hyperactivated cells, GSDMD pores cause membrane permeabilization to release IL-1 cytokines, which lack the N-terminal signal peptide (leaderless) required for the conventional pathway of vesicular protein release through the endoplasmic reticulum–Golgi network (21). However, while the GSDMD pore serves as a bona fide conduit for IL-1 release during hyperactivation, proteins may leak out nonspecifically through lysed membranes during pyroptosis (19, 22). To study the mechanism of IL-1 transport via the GSDMD pore, we refer specifically to hyperactivation rather than pyroptosis as the cellular context. Recent research sheds light on the importance of electrostatics in IL-1 release (17, 23). Here, we modeled computationally the pore-dependent IL-1 release and discovered pore-extrinsic factors influencing release rates.

Results

Coarse-Grained Modeling of GSDMD-Dependent IL-1β Transport. Membrane binding is required for GSDMD pore formation. GSDMD-NT selectively binds to phosphatidylinositol phosphates, phosphatidylserine (PS), and phosphatidic acid, which are mainly on the inner leaflet of the mammalian cell membrane, and to cardiolipin, a lipid present in mitochondrial and bacterial membranes (6, 9). These lipids are collectively known as acidic lipids due to their negatively charged head groups. Consistently, cryo-electron microscopy studies identified three positively charged patches, or basic patches (BPs), in the membrane-facing side of the pore that interacts with acidic lipids (17, 24) (Fig. 1*A*). By contrast, the conduit side of the pore is predominantly negatively charged, owing to the presence of negatively charged patches, or acidic patches (APs) (17)

Significance

Gasdermin D (GSDMD) forms large pores that channel the release of alarmins, including interleukin-1 (IL-1) family cytokines, from living cells. IL-1 is synthesized as an inactive cytosolic precursor known as pro-IL-1, which is proteolytically processed into the active mature IL-1 in response to inflammasome activation or other physiological or pathological stimuli. GSDMD pores preferentially release mature IL-1 over pro-IL-1 despite their similar molecular dimensions, both markedly smaller than the pore, indicating that factors beyond size may affect the transport. Our investigation into the role of electrostatics in this preferential release revealed a charge-based gating mechanism for GSDMD pores. Our studies have broad implications in GSDMD-mediated inflammation and contribute to understanding of how large transmembrane pores may achieve cargo preference.

Author contributions: W.J.X., S.X., A.W., and H.W. designed research; W.J.X. and S.X. performed research; W.J.X. and S.X. contributed new reagents/analytic tools; W.J.X., S.X., A.W., and H.W. analyzed data; and W.J.X., S.X., A.W., and H.W. wrote the paper.

Reviewers: M.G., University of California San Francisco; and Y.W., Albert Einstein College of Medicine.

The authors declare no competing interest.

[1]W.J.X. and S.X. contributed equally to this work.

[2]To whom correspondence may be addressed. Email: warshel@usc.edu or wu@crystal.harvard.edu.

This article contains supporting information online at http://www.pnas.org/lookup/suppl/doi:10.1073/pnas.2120287119/-/DCSupplemental.

Published February 3, 2022.

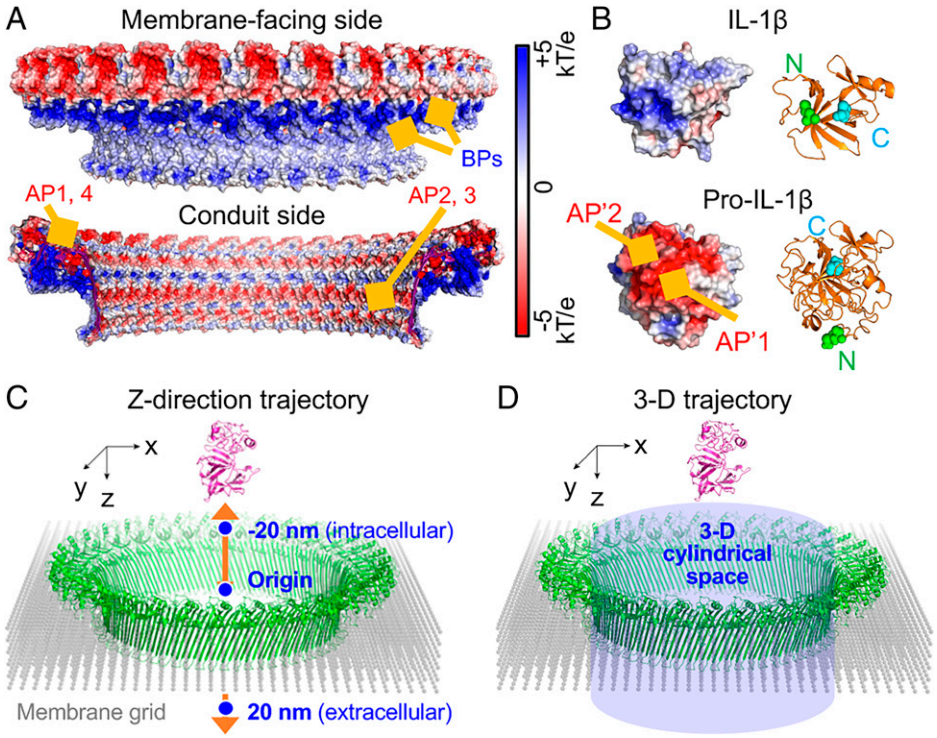

Fig. 1. Coarse-grained models of the transport of IL-1β. (*A*) Intracellular and membrane-facing views of the GSDMD pore showing electrostatic potential surfaces from −5 to +5 kT/e. Locations of GSDMD BPs (blue) and APs (red) are indicated. (*B*) Surface electrostatic potentials of pro-IL-1β model and mature IL-1β structure from −5 to +5 kT/e. Locations of APs (red) on the surfaces of the cargoes are indicated. Ribbon diagrams are shown for the two structurally aligned cargoes, with N termini indicated as green spheres and C termini cyan spheres. (*C* and *D*) Schematics of coarse-grained modeling of the cargo transport through the pore. Two scenarios are considered: cargo moving along the pore central axis (*z* axis) from −20 (intracellular) to +20 (extracellular) nm (*C*) and cargo moving in the 3D cylindrical space within the pore (*D*).

(Fig. 1*A*). Previously, we provided evidence by mutagenesis that these APs electrostatically filter out pro-IL-1β, a negatively charged cargo, while allowing the passage of IL-1β, which is devoid of the small acidic prodomain (17, 23) (Fig. 1*B*).

Despite knowledge of the lipid preferences of GSDMD, it is unknown whether the interaction between GSDMD and lipids indirectly influences IL-1β transport. We hypothesized that membrane lipids could considerably modulate the electrostatic environment cargoes experience because acidic lipids may neutralize the positive charges of the GSDMD pore (25, 26) and affect the electrostatic environment within the pore. To this end, we employed computational modeling to explore the IL-1β transport process through a membrane-integrated GSDMD pore (*SI Appendix*). The large size of the system necessitated the use of a coarse-grained model of the pore embedded into a membrane grid to reduce computational cost (Fig. 1 *C* and *D*). The membrane particles near the BPs of the pore were assigned various negative charges based on the lipid-binding degree (LBD) of GSDMD (see a detailed picture in *SI Appendix*, Fig. S1). The GSDMD pore and membrane particles together form the surrounding environment for cargoes. The pore was oriented with a horizontal cross-section as the *xy* plane, the pore center-of-mass as the origin, and the pore central axis as the *z* axis. To further minimize computational burden, we first used the central *z* axis as the hypothetical cargo pathway to perform the majority of our simulations. In this case, the cargoes were moved along the central *z* axis in one dimension to simulate the transport process, and the orientations were randomly chosen for the cargoes to obtain averaged results (Fig. 1*C*). For validation purposes, we also simulated the movement of pro-IL-1β and mature IL-1β in three dimensions through a cylindrical space covering the pore conduit (Fig. 1*D*). Details of model construction can be found in *SI Appendix*.

GSDMD–Membrane Interaction Allows the Preferential Release of Mature IL-1β. The large GSDMD pore provides a confined aqueous environment for cargo transport, where salt would screen the electrostatic interaction. The simplest way to estimate the electrostatics might be to calculate the electric field within the pore by solving the Poisson–Boltzmann equation. However, it is difficult to study the effect of acidic lipids by solving the equation, and the estimated electrostatics within the pore should be quite small. The magnitude of the electrostatics is largely controlled by the Debye length, which is 0.78 nm at a presumed physiological salt (NaCl) concentration of 0.15 M estimated from Debye–Hückel theory. Considering that acidic lipids may substantially modulate ion distribution around the GSDMD pore, calibration of the electrostatic screening is essential to rationalize experimental results. Here, we used the electrostatic screening factor of $f_{ij} = \exp(-r_{ij} * \alpha * \sqrt{I})$ for each pair of atoms *i* and *j* in the free-energy (FE) calculation, where r_{ij} is the distance between the two atoms in Å, *I* is the salt concentration in molar, and α is the screening factor with a value of 0.11, which was initially parameterized to reproduce protein folding energy in electrolytes (27). Under this condition, the screening factor corresponds to an effective Debye length of 2.3 nm in 0.15 M salt. Here, as we show below, the Debye length of 2.3 nm not only reproduces well the previous experimental findings (17), but also yields a prediction for the effect of salt concentration we further validated with a liposome assay.

The FE profile of the cargo traveling through the GSDMD pore provides a quantitative measure of the energetics. Therefore, we calculated the FE (in kcal/mol) as a function of the LBD of GSDMD, with zero indicating no electrostatic interaction between GSDMD and the membrane and one meaning all positively charged residues in the BPs of the pore are effectively neutralized by acidic lipids in the membrane (*SI Appendix*).

The FE is expressed as $\Delta G = 332\Sigma_{i,j}\frac{Q_iQ_j}{r_{ij}\varepsilon_{\text{eff}}}f_{ij}$, where Q_i and Q_j with unit in elementary charge run over cargo and the surrounding environment (GSDMD pore plus membrane grid), respectively; r_{ij} is the distance between the two atoms in Å; f_{ij} is the screening factor explained above; and ε_{eff} is set to 78, the dielectric constant of water, to mimic the aqueous environment (27, 28).

We first modeled the transport of wild-type pro-IL-1β and mature IL-1β through the wild-type GSDMD pore at 0.15 M salt (Figs. 1*B* and 2 *A* and *B*). Surprisingly, from an LBD value of zero to one, the interaction between pro-IL-1 and GSDMD shifts from attraction (FE < 0) to repulsion (FE > 0) (Fig. 2*A*). The shift is due to a negative charge of pro-IL-1β [−11.3 e; estimated by the Monte Carlo proton transfer algorithm (27)], a positive charge of GSDMD at LBD 0 (+122.4 e), and an effectively negative charge of GSDMD after the lipid-binding residues counterbalanced by the membrane at LBD 1 (−273.6 e). By contrast, mature IL-1β has a weak electrostatic interaction with the pore, regardless of the LBD of GSDMD (Fig. 2*B*), consistent with the weakly basic nature (+1.0 e) of mature IL-1β. Therefore, LBD of GSDMD strongly influences the repulsive or attractive nature of the electrostatic interaction between GSDMD and pro-IL-1β. To enable the preferential release of IL-1β over pro-IL-1β, GSDMD needs to interact extensively with the membrane (or high LBD; see quantification in the next section).

Besides the two wild-type systems, we performed in silico mutation of the negatively charged residues in GSDMD APs (AP1 and AP2; five and two Asp/Glu residues, respectively; Fig. 1*A*) to alanine and assessed the release of wild-type pro-IL-1β through the charge-mutant pores (Fig. 2 *C* and *D*). The alanine mutations weaken the repulsion of pro-IL-1β at high LBD and strengthen the attraction of pro-IL-1β at low LBD, with the AP1 mutation having a more pronounced effect than AP2 (Fig. 2 *C* and *D*). In addition, we kept GSDMD as wild type and mutated the negatively charged residues in pro-IL-1β AP′s (AP1′ and AP2′; 8 and 11 Asp/Glu residues to Lys, respectively; Fig. 1*B*). As expected, the FE values flipped from attractive to repulsive at low LBD and from repulsive to attractive at high LBD (Fig. 2 *E* and *F*). These simulation data at high LBD agree with the experimental data by mutagenesis (17) and explain the more promiscuous release of pro-IL-1β from the AP1 and AP2 mutant pores.

Kinetic Simulation Reveals the Extent of GSDMD–Membrane Interaction. To quantitatively deduce an LBD value that may account for previous experimental observations (17), we performed kinetic simulations to calculate the release rate of IL-1β or pro-IL-1β in the six transport systems (Fig. 2) with different forms of the GSDMD pore and the cargo (Fig. 3). The simulation aims to numerically solve a master equation, which is the minimalist model here (*SI Appendix*). The master equation writes $P_{x,T+1} = \frac{1}{2}P_{x-\Delta x,T} * p_{\text{accept}}[x - \Delta x \to x] + \frac{1}{2}\ P_{x+\Delta x,T} * p_{\text{accept}}[x + \Delta x \to x]$, where $P_{x,T}$ is the probability of finding cargo at site x at time T, Δx is the spacing, the coefficient of $\frac{1}{2}$ represents the equal probability to move forward and backward, and the Metropolis acceptance ratio p_{accept} as the transition rate ensures that the system follows Boltzmann distribution.

We simulated cargo passing through the pore axis (z axis) from above the pore (−20 nm; intracellular) to below the pore (20 nm; extracellular) under the influence of FE. The average number of Monte Carlo steps to first reach the 20-nm position is defined as the mean first-passage time (T_{MFPT}), and the cargo release rate is measured as $1/T_{\text{MFPT}}$. Considering that relative rates are informative in comparing the different systems, the release rates were normalized to the largest value. The normalized rates are termed "relativerate" (Fig. 3). We attributed the different relative rates to electrostatic interactions considering similar cargo sizes.

Our simulations demonstrated that the cargo release rates are contrasting at high LBD values (~0.8 to 1), with mature IL-1β through the wild-type GSDMD pore at the fastest rate, pro-IL-1β through the wild-type GSDMD pore at the slowest, and intermediate rates corresponding to the systems involving charge-mutant GSDMD or pro-IL-1β (Fig. 3). This order is consistent with our previous experimental results on IL-1β transport through GSDMD pores that demonstrated repulsion of pro-IL-1β (17). Importantly, the release rates are virtually indistinguishable at low LBD values (approximately less than

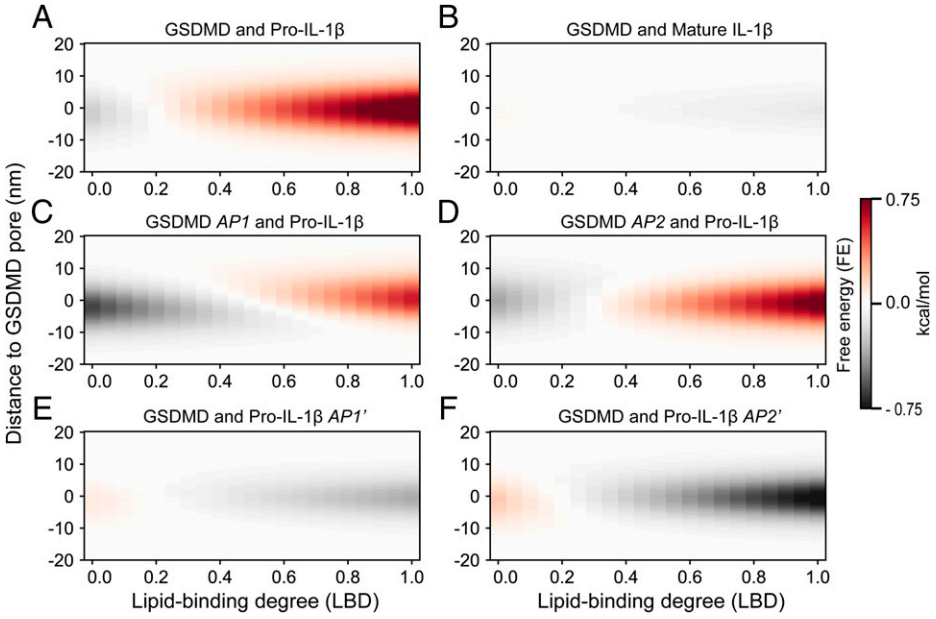

Fig. 2. GSDMD–membrane interaction modulates IL-1 transport. The FE is calculated as a function of the LBD of GSDMD for six scenarios. (*A* and *B*) Transport of pro-IL-1β (*A*) and mature IL-1β (*B*) through the GSDMD pore. (*C* and *D*) Transport of pro-IL-1β through AP1-mutant (*C*) and AP2-mutant (*D*) GSDMD pores. (*E* and *F*) Transport of AP1′-mutant (*E*) and AP2′-mutant (*F*) pro-IL-1β through the GSDMD pore.

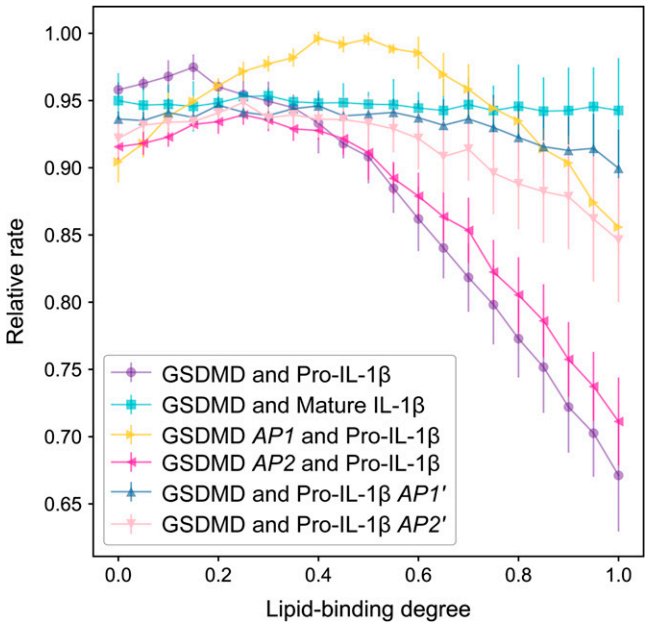

Fig. 3. Cargo release rates vary with GSDMD–membrane interaction. Rates are represented as the reverse of the MFPT for simulated cargo transport through the pore. The rates are then normalized to the largest value to get the relative rate. Error bars represent SDs for 10 random cargo orientations for each system.

0.4). These results together indicate that electrostatics are responsible for the preferential release of mature IL-1β over pro-IL-1β and that high LBD is required for effective neutralization of positive charges in GSDMD to achieve electrostatic filtering against pro-IL-1β.

Comparison between the relative release rates obtained experimentally (17) and computationally (Fig. 3) suggested that LBD in reality should be close to one. Assuming an LBD value of one, the FE barrier for pro-IL-1β going through the pore along its central axis is 0.94 kcal/mol (Fig. 2*A*), whereas that for mature IL-1β is nearly negligible (Fig. 2*B*). As shown below, this FE barrier increases significantly when pro-IL-1β is simulated to deviate from the pore's central axis. This distinction provides computational evidence for the electrostatics-mediated preferential release of IL-1β through the GSDMD pore.

Salt Attenuates the Electrostatic Filtering Effect. In contrast to extensive lipid interaction at the BPs, the pore conduit of GSDMD is situated in an aqueous environment. We further compared the FE of pro-IL-1β and mature IL-1β interacting with GSDMD at salt concentrations of 0.05 M and 0.15 M (Fig. 4*A*), at which both GSDMD and IL-1β cargoes were experimentally stable. In the following modeling, LBD was approximated as one based on conclusions from kinetic simulations (Fig. 3). The effect of salt was realized by scaling FE by the factor f_{ij} (27) (above section and *SI Appendix*).

At 0.15 M salt concentration, the energy landscape of mature IL-1β is essentially flat, while that of pro-IL-1β demonstrates a significant barrier of 0.94 kcal/mol, consistent with results from LBD analyses (Fig. 2). Surprisingly, the barrier of pro-IL-1β traveling through the pore at 0.05 M salt concentration is ∼7 times that at 0.15 M salt concentration, indicating that salt has a remarkable effect on the electrostatic repulsion exerted by GSDMD on pro-IL-1β. By contrast, although there is potentially a shallow energy well for mature IL-1β at either salt concentration, the energy landscape of mature IL-1β does not strongly vary with salt. Consistently, Monte Carlo simulations for pro-IL-1β at 0.05 M salt concentration did not converge within the simulation time, which suggests a negligible release rate, whereas those for mature IL-1β showed a rate highly similar to that at 0.15 M (0.86 times) (Fig. 4*B*). Overall, rate dependence on salt concentration of pro-IL-1β transport also indicates electrostatic filtering.

We then asked how far from the pore electrostatic effect against pro-IL-1β may extend in a physiological environment. To calculate a characteristic "shielding length" of the pore, we used a simple mathematical model, $\Delta G \propto \exp(-z/L)$, where ΔG is FE, z is the distance between the cargo and the pore center, and L is the characteristic shielding length. We then plotted this equation in its logarithmic form to perform linear regression fitting, in which the slope of the fitted line is $-1/L$ (Fig. 4*C*). The calculated value of L is −3.2 nm, suggesting that pro-IL-1β starts to experience significant repulsion when it is ∼3.2 nm away from the pore center on the intracellular side, which roughly aligns with the rim of the pore.

Lastly, we performed liposome-based experiments in the presence of 0.05 M or 0.15 M salt concentration to check these computational findings (Fig. 4*D* and *SI Appendix*). Briefly, we loaded freshly purified monomeric pro-IL-1β and mature IL-1β into PS-containing liposomes. We then added purified MBP-tagged GSDMD containing a human rhinovirus 3C protease (3C) cleavage site (for simplicity, GSDMD) and the activating enzyme (En, which includes a tobacco etch virus protease [TEV] that cleaves off MBP and 3C that cleaves off GSDMD-CT) to the liposome suspension at a sublytic concentration to assess cargo release through GSDMD pores. Mature IL-1β was robustly released from the liposomes into the external buffer at either salt concentration, consistent with the lack of a significant energetic barrier predicted computationally. Mature IL-1β has a faster release rate at the higher salt concentration, in agreement with computational predictions (Fig. 4*B*). By contrast, while pro-IL-1β was modestly released at 0.15 M salt concentration over a 2-h time window, it was kept virtually entirely in the liposomes at 0.05 M salt concentration, indicating that a low-salt environment amplifies the energetic barrier for pro-IL-1β. Therefore, the liposome experiment indicates a more pronounced electrostatic barrier for pro-IL-1β going through the pore at a lower salt concentration. This consistency between computational and experimental results again highlights the importance of electrostatic filtering in pro-IL-1β release.

Three-Dimensional Modeling Demonstrates Thwarted Transport of Pro-IL-1β. In consideration of computational cost, the above computations were performed by using the pore central axis as the simplified hypothetical cargo trajectory (Fig. 1*C*). However, the electrostatic field within the pore conduit decays toward the center, rather than being uniform (Fig. 5*A*). We therefore further validated our findings by whole-pore simulations of pro-IL-1β and mature IL-1β transport at 0.15 M salt concentration in a three-dimensional (3D) space (Fig. 1*D*). As shown in a representative trajectory, mature IL-1β experienced small energy wells during its exit through the pore in less than 30,000 Monte Carlo steps on average (Fig. 5*B*). By contrast, pro-IL-1β was largely retained at the intracellular side ($z < 0$) of the pore until the energy barrier was overcome at around 75,000 steps on average. The mean-first passage times (MFPTs) for pro-IL-1β and mature IL-1β among 1,000 whole-pore simulations are 73,135 ± 72,870 and 27,528 ± 22,365 Monte Carlo steps, respectively. A statistics of cargo behavior on the pore *xy* plane is shown in *SI Appendix*, Fig. S2. Based on this 3D transport system, the release rate of pro-IL-1β is, on average, 0.38 times that of mature IL-1β, which again supports the preferential release of mature IL-1β.

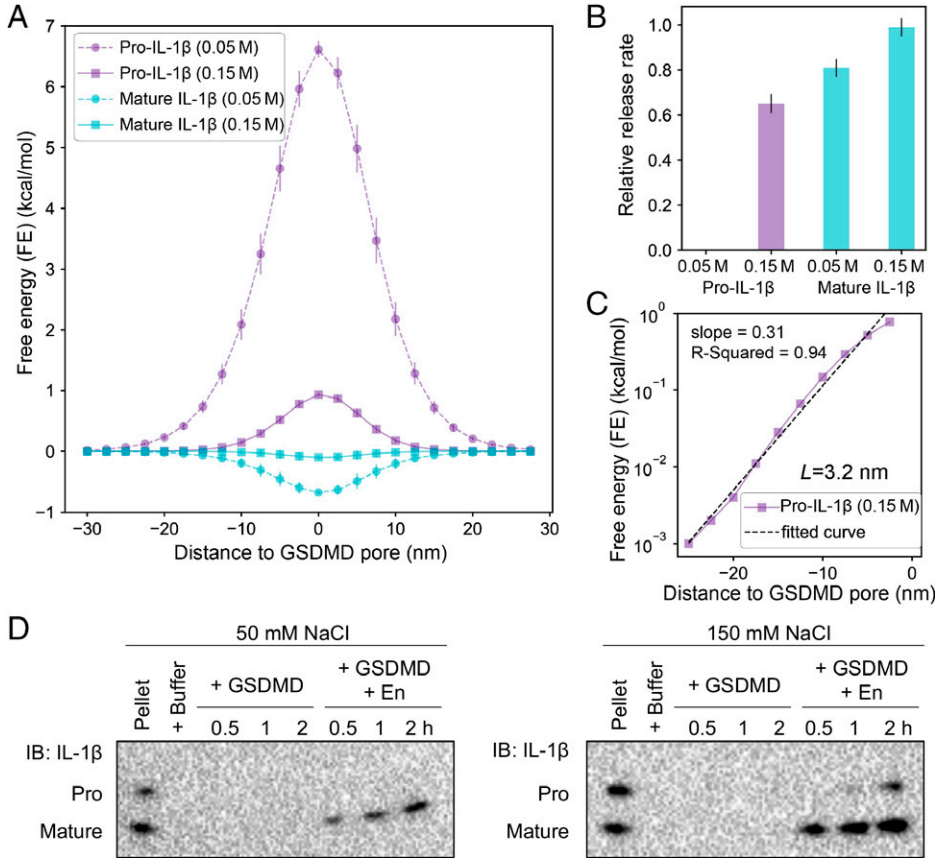

Fig. 4. Salt diminishes the difference in FE between pro-IL-1β and mature IL-1β. (*A*) Energy landscape of pro-IL-1β and mature IL-1β as they travel through the GSDMD pore at two salt concentrations, 0.05 M and 0.15 M. (*B*) Relative release rate. (Definition is the same as Fig. 3.) Error bars in *A* and *B* were obtained by averaging over 10 random cargo orientations. (*C*) Calculation of the characteristic shielding length of the GSDMD pore. FE values for pro-IL-1β at 0.15 M were used. With the logarithmic of the FE as the vertical axis and *z* as the horizontal axis, the slope is −1/L. (*D*) Immunoblots of pro-IL-1β and mature IL-1β released through GSDMD pores from liposomes at two salt environments (0.05 M and 0.15 M) over 2-h time windows.

An Uncalibrated Debye Length Does Not Explain Electrostatic Filtering. To further elucidate whether a calibrated Debye length, possibly due to the pore environment, such as the embedding into acidic lipids, is crucial for modeling electrostatic filtering, we performed 3D kinetic simulations at two different Debye lengths. Our electrostatic screening factor used in the calculation thus far corresponds to an effective Debye length of 2.3 nm, while the value of 0.78 nm corresponds to that estimated with Debye–Hückel theory. As seen from *SI Appendix*, Fig. S3, the Debye length of 0.78 nm does not show selectivity or explain the experiment because of the underestimated electrostatics.

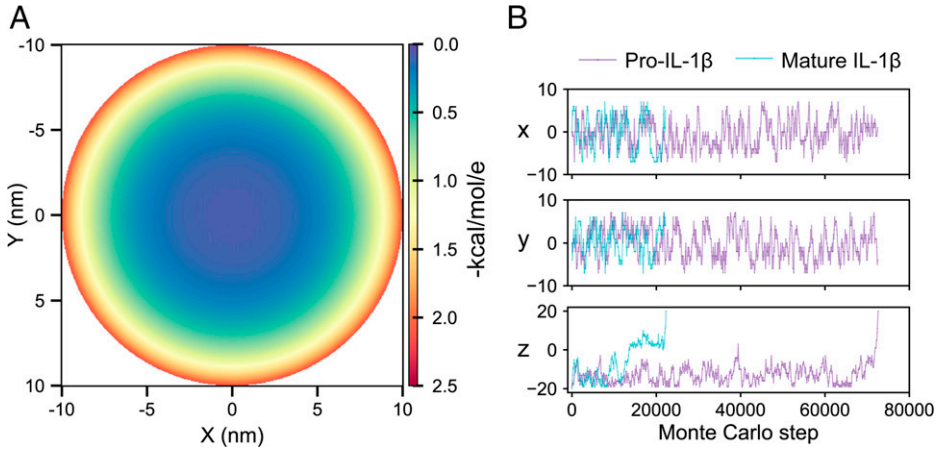

Fig. 5. The 3D modeling reveals preferential release of mature IL-1β. (*A*) The electric field distribution of the GSDMD pore conduit, shown using a cross-section of the pore at the midpoint of the *z* height (z = 0). The electric field at an indicated point in the conduit was calculated as the electrostatic interaction FE (Δ*G*) for an elementary charge of e with units in kcal/mol/e. (*B*) A representative 3D trajectory of pro-IL-1β and mature IL-1β projected to the cross-section of the pore (*x* and *y* directions) and central axis of the pore (*z* direction).

We also performed one-dimensional (1D) simulations with cargo at different locations (x, y) in the xy plane. The reasons for this exercise are the nonhomogeneous electrostatics within the pore and the preferential sampling of pro-IL-1β and mature IL-1β molecules on the pore region away from the pore center (*SI Appendix*, Fig. S2). For a Debye length of 2.3 nm, the electrostatic potential becomes much stronger when cargo moves from the center to the periphery, with interaction FE of 1.3 kcal/mol at (3, 0) nm and 3.4 at (6, 0) nm [(0, 0) is the center] (*SI Appendix*, Fig. S4). Consequently, the selectivity between pro-IL-1β and mature IL-1β becomes higher (*SI Appendix*, Table S1). The result is consistent with the finding that 3D simulation (Fig. 5*B*) shows a higher selectivity than the 1D simulation (Fig. 2). However, the electrostatic potential and interaction FE are small with a Debye length of 0.78 nm, even along off-center paths (*SI Appendix*, Fig. S5). At the extreme position of (7, 0) nm in the xy plane, where one side of the cargo is close to abutting the pore, the interaction FE remains small. Correspondingly, there is no selectivity for a Debye length of 0.78 nm, as seen from the kinetic simulation (*SI Appendix*, Table S2).

Estimation of the Time Scale for Unfiltered Single Cargo Release. To offer an additional insight for cargo release from GSDMD pores, we sought to calculate the time scale for cargo release both from experimental data and theoretically. Our published data showed that the initial release rate of mature IL-1β from liposomes is 294% per hour, or 0.082% per second (17). With an assumed average liposome radius of 1 μm, lipid concentration of 1 mM, mature IL-1β concentration of 1 μM, GSDMD monomer concentration of 0.5 μM, and 33 protomers per pore (*SI Appendix*, Tables S3 and S4), each liposome would contain 2,500 cargo molecules and 750 pores, leading to the time of 0.48 s for one cargo molecule to escape from the liposome.

Theoretically, we consider cargo release from a liposome as a two-step process, Brownian motion within the liposome to reach the membrane (with certain probability of arriving at a pore) and the act of going through the GSDMD pore (*SI Appendix*, Fig. S6). For mature IL-1β, we believe that its rate of release depends mainly on Brownian diffusion to find a pore conduit, considering that it does not encounter an energy barrier through the pore. This calculated, diffusion-controlled IL-1β release rate is 0.09 s from a 1-μm radius liposome containing 750 pores (*SI Appendix*). The excellent agreement between the theoretical calculation and the experimental data suggests that the Brownian motion within liposome sets the time scale of cargo release in the absence of an energy barrier.

Discussion

Our study highlights the role of GSDMD as an electrostatic filter that energetically permits the release of mature IL-1β and deters the passage of pro-IL-1β. This selectivity is largely determined by the passage through the GSDMD pore per se, as the Brownian diffusion to find the pore should be consistent among the tested cargoes with similar sizes. Besides the intrinsic charges carried by GSDMD and the cargoes, we demonstrated the electrostatic influence exerted by GSDMD–membrane interaction and salt using coarse-grained models and kinetic simulations. We found that interaction between GSDMD and acidic lipids can broaden the difference in FE between pro-IL-1β and mature IL-1β to allow deterrence against pro-IL-1β, whereas high salt diminishes the energy difference to permit more promiscuous leakage of pro-IL-1β. These effects suggest the possibility that distribution of lipids in the membrane and electrolytes near the membrane may be tuned to modulate GSDMD-mediated electrostatic filtering.

A Debye length larger than that estimated using Debye–Hückel theory was necessary to account for the experimental observations. The exact mechanistic source for the elongated Debye length is unclear, but this Debye length could suggest that the ion concentration within the membrane-embedded GSDMD pore conduit may be different from bulk solution. One possibility is that the charged lipids form an ion-depletion layer around the membrane (29, 30), likely due to ion concentration tuning by the negatively charged lipids around the pore. The implications here require further examination, and new spectroscopy methods may be needed to measure the local ion concentration within the pore. It is interesting that a Debye length parameterized for protein folding (28) was also applicable to modeling the electrostatics of the GSDMD pore. This might not be surprising because, given the comparable sizes of the protein cargoes and the pore, the in-pore electrostatics may significantly deviate from the bulk solution as the cargoes approach the pore periphery. For additional studies, it will be important to tune this value to further improve the match to experimental data, and we may find that a minimally elongated Debye length is sufficient.

There may be several reasons that our calculation underestimates the electrostatic discrimination between pro- IL-1β and mature IL-1β. In the kinetics simulation, we first studied the cargo release through the pore center, where electrostatics is weaker than that at the periphery of the pore. It is anticipated that a stronger selectivity may be obtained when the whole pore is considered, especially given the larger area toward the periphery of the pore. This was indeed the case when we modeled cargo release in three dimensions; however, these calculations likely still underestimate the selectivity because we used a reflecting boundary condition in the rate calculation to avoid the cargo diffusing back into the liposome. Such a boundary condition favors the release of pro-IL-1β relative to IL-1β because it reflects the former back to the pore more often than it does the latter. Improving the above points could additionally reach a better agreement with the experiment.

Finally, it will be important to examine the cargo preferences of different GSDM pores at specific cellular locations. Not only do GSDMs have nonidentical charge features, as AP1 is conserved in the family, while the negatively charged residues in AP2, AP3, and AP4 can be offset by nearby positively charged residues (17), but GSDMs may also have different LBDs and shielding strengths based on local concentrations of acidic lipids and salt, respectively. It is likely that cargo preference is specific to each GSDM pore and the cellular environment in which the pore forms.

Materials and Methods

Structure and Electrostatics Analysis. We used PyMOL and the Adaptive Poisson–Boltzmann Solver plug-in to analyze the structures and electrostatics of GSDMD (Protein Data Bank [PDB] ID code 6VFE), IL-1β (PDB ID code 8I1B), and pro-IL-1β (model generated by using I-TASSER based on IL-1β crystal structure). We performed in silico mutagenesis using the MOLARIS-XG (version 9.15) simulation package (31).

Setup of Cargo Transport Model. We constructed coarse-grained models of the GSDMD pore and IL-1β cargoes using MOLARIS-XG (version 9.15) (31). To mimic membrane interaction, we immersed the pore into a membrane grid with assigned negative charges to grid points near the pore assigned negative charges to grid points near the pore. We modeled cargo transport as a 1D process along the z axis and as a 3D process covering the entire pore conduit.

Calculation of FE. The whole GSDMD–membrane system was used to calculate FE during cargo transport. FEs in kcal/mol were calculated as $\Delta G = 332\Sigma_{i,j}\frac{Q_iQ_j}{r_{ij}\varepsilon_{\text{eff}}}f_{ij}$ (28). The electrostatic screening factor f_{ij} was used to account for salt effects. A calibrated Debye length of 2.3 nm was used in the majority of our simulations.

Calculation of Cargo Release Rate. We performed Monte Carlo kinetics simulations to quantify cargo release rates. The cargo release rate is quantified as the reverse of MFPT (32), whose unit is the number of Monte Carlo steps. At the starting and ending point of the pore, we used a reflecting boundary condition and an adsorbing boundary condition, respectively.

Molecular Cloning. Human GSDMD coding sequence, with residues 259 through 275 replaced by the cleavage site of 3C (LEVLFQ/GP), was cloned into the pDB.His.MBP vector to append a TEV-removable His6-MBP tag at the N terminus. Murine IL-1β was cloned into a pET28a vector following the N-terminal His6-SUMO tag.

Protein Purification. GSDMD and IL-1β were expressed in *Escherichia coli* BL21 (DE3) and BL21 (DE3) RipL cells, respectively, and enriched by using Ni–nitrilotriacetic acid (NTA) beads (Qiagen). Eluates containing MBP-GSDMD was further purified by using the Superdex 200 (10/300) column (GE Healthcare Life Sciences). The His_6-SUMO tag of IL-1β was cleaved off on an Ni-NTA column by using His6-tagged ULP1 protease. Flowthrough containing IL-1β was further purified by using the Superdex 75 (10/300) column (GE Healthcare Life Sciences).

GSDMD-Dependent IL-1β Release from Liposomes. We loaded freshly purified IL-1β into liposomes containing 25% 1,2-dioleoyl-*sn*-glycero-3-phospho-l-serine (PS). We treated the liposomes with purified MBP-GSDMD at a previously determined sublytic concentration (17). Pore formation was triggered by the addition of TEV and 3C. At indicated time points during a 2-h window, liposome pellets and supernatants were collected for standard immunoblotting.

Data Availability. The MOLARIS-XG package is available upon request from the University of Southern California. Molecular coordinates are available at the PDB (ID codes 6VFE and 8I1B). Codes to simulate the kinetics are available at GitHub (https://github.com/Wenjun-Xie/kinetics_in_pore). All study data are included in the article and/or *SI Appendix*.

ACKNOWLEDGMENTS. This work was supported by NIH Grants R01AI139914 (to H.W.) and R35GM122472 (to A.W.); and NSF Grant MCB-1707167 (to A.W.). We thank members of the H.W. and A.W. laboratories, Andrew Kruse, Maofu Liao, and Stephen Blacklow for helpful discussions.

1. X. Liu, S. Xia, Z. Zhang, H. Wu, J. Lieberman, Channelling inflammation: Gasdermins in physiology and disease. *Nat. Rev. Drug Discov.* **20**, 384–405 (2021).
2. S. Xia, L. R. Hollingsworth IV, H. Wu, Mechanism and regulation of gasdermin-mediated cell death. *Cold Spring Harb. Perspect. Biol.* **12**, a036400 (2020).
3. P. Broz, P. Pelegrín, F. Shao, The gasdermins, a protein family executing cell death and inflammation. *Nat. Rev. Immunol.* **20**, 143–157 (2020).
4. Z. Zhang *et al.*, Gasdermin E suppresses tumour growth by activating anti-tumour immunity. *Nature* **579**, 415–420 (2020).
5. Z. Zhou *et al.*, Granzyme A from cytotoxic lymphocytes cleaves GSDMB to trigger pyroptosis in target cells. *Science* **368**, eaaz7548 (2020).
6. J. Ding *et al.*, Pore-forming activity and structural autoinhibition of the gasdermin family. *Nature* **535**, 111–116 (2016).
7. Z. Liu *et al.*, Crystal structures of the full-length murine and human gasdermin D reveal mechanisms of autoinhibition, lipid binding, and oligomerization. *Immunity* **51**, 43–49.e4 (2019).
8. C. Rogers *et al.*, Gasdermin pores permeabilize mitochondria to augment caspase-3 activation during apoptosis and inflammasome activation. *Nat. Commun.* **10**, 1689 (2019).
9. X. Liu *et al.*, Inflammasome-activated gasdermin D causes pyroptosis by forming membrane pores. *Nature* **535**, 153–158 (2016).
10. J. Shi *et al.*, Cleavage of GSDMD by inflammatory caspases determines pyroptotic cell death. *Nature* **526**, 660–665 (2015).
11. N. Kayagaki *et al.*, Caspase-11 cleaves gasdermin D for non-canonical inflammasome signalling. *Nature* **526**, 666–671 (2015).
12. W. T. He *et al.*, Gasdermin D is an executor of pyroptosis and required for interleukin-1β secretion. *Cell Res.* **25**, 1285–1298 (2015).
13. N. Kayagaki *et al.*, NINJ1 mediates plasma membrane rupture during lytic cell death. *Nature* **591**, 131–136 (2021).
14. E. Bjanes *et al.*, Genetic targeting of Card19 is linked to disrupted NINJ1 expression, impaired cell lysis, and increased susceptibility to Yersinia infection. *PLoS Pathog.* **17**, e1009967 (2021).
15. J. Shi, W. Gao, F. Shao, Pyroptosis: Gasdermin-mediated programmed necrotic cell death. *Trends Biochem. Sci.* **42**, 245–254 (2017).
16. S. Rühl *et al.*, ESCRT-dependent membrane repair negatively regulates pyroptosis downstream of GSDMD activation. *Science* **362**, 956–960 (2018).
17. S. Xia *et al.*, Gasdermin D pore structure reveals preferential release of mature interleukin-1. *Nature* **593**, 607–611 (2021).
18. D. Zhivaki, J. C. Kagan, Innate immune detection of lipid oxidation as a threat assessment strategy. *Nat. Rev. Immunol.*, 10.1038/s41577-021-00618-8 (2021).
19. C. L. Evavold *et al.*, The pore-forming protein gasdermin D regulates interleukin-1 secretion from living macrophages. *Immunity* **48**, 35–44.e6 (2018).
20. R. Heilig *et al.*, The gasdermin-D pore acts as a conduit for IL-1β secretion in mice. *Eur. J. Immunol.* **48**, 584–592 (2018).
21. A. H. Chan, K. Schroder, Inflammasome signaling and regulation of interleukin-1 family cytokines. *J. Exp. Med.* **217**, e20190314 (2020).
22. K. Phulphagar *et al.*, Proteomics reveals distinct mechanisms regulating the release of cytokines and alarmins during pyroptosis. *Cell Rep.* **34**, 108826 (2021).
23. M. Monteleone *et al.*, Interleukin-1β maturation triggers its relocation to the plasma membrane for gasdermin-D-dependent and-independent secretion. *Cell Rep.* **24**, 1425–1433 (2018).
24. J. Ruan, S. Xia, X. Liu, J. Lieberman, H. Wu, Cryo-EM structure of the gasdermin A3 membrane pore. *Nature* **557**, 62–67 (2018).
25. D. Murray *et al.*, Electrostatic properties of membranes containing acidic lipids and adsorbed basic peptides: Theory and experiment. *Biophys. J.* **77**, 3176–3188 (1999).
26. L. Li, X. Shi, X. Guo, H. Li, C. Xu, Ionic protein-lipid interaction at the plasma membrane: What can the charge do? *Trends Biochem. Sci.* **39**, 130–140 (2014).
27. I. Vorobyov, I. Kim, Z. T. Chu, A. Warshel, Refining the treatment of membrane proteins by coarse-grained models. *Proteins* **84**, 92–117 (2016).
28. I. Muegge, T. Schweins, A. Warshel, Electrostatic contributions to protein-protein binding affinities: Application to Rap/Raf interaction. *Proteins* **30**, 407–423 (1998).
29. K. Kim, Migration of ions near charged surface. *PLoS One* **16**, e0250343 (2021).
30. A. K. Khitrin, K. A. Khitrin, M. A. Model, A model for membrane potential and intracellular ion distribution. *Chem. Phys. Lipids* **184**, 76–81 (2014).
31. A. Warshel *et al.*, Molaris-XG (University of Southern California, Los Angeles, 2012).
32. N. F. Polizzi, M. J. Therien, D. N. Beratan, Mean first-passage times in biology. *Isr. J. Chem.* **56**, 816–824 (2016).